

# Pre- and post-treatment image-based dosimetry in $^{90}\text{Y}$ -microsphere radioembolization using the TOPAS Monte Carlo toolkit

Alejandro Bertolet<sup>1</sup> , Eric Wehrenberg-Klee<sup>2</sup> , Mislav Bobić<sup>1,3</sup> , Clemens Grassberger<sup>1</sup> , Joseph Perl<sup>4</sup> , Harald Paganetti<sup>1</sup>  and Jan Schuemann<sup>1</sup> 

<sup>1</sup> Department of Radiation Oncology, Massachusetts General Hospital and Harvard Medical School, Boston, MA, United States of America

<sup>2</sup> Department of Radiology, Division of Interventional Radiology, Massachusetts General Hospital, Boston, MA, United States of America

<sup>3</sup> Department of Physics, ETH Zürich, Zürich, Switzerland

<sup>4</sup> SLAC National Accelerator Laboratory, Menlo Park, CA, United States of America

E-mail: [abertoletreina@mgh.harvard.edu](mailto:abertoletreina@mgh.harvard.edu)

**Keywords:**  $^{90}\text{Y}$  microsphere, topas, internal dosimetry, radionuclides, radioembolization

## Abstract

**Objective.** To evaluate the pre-treatment and post-treatment imaging-based dosimetry of patients treated with  $^{90}\text{Y}$ -microspheres, including accurate estimations of dose to tumor, healthy liver and lung. To do so, the Monte Carlo (MC) TOPAS platform is in this work extended towards its utilization in radionuclide therapy. **Approach.** Five patients treated at the Massachusetts General Hospital were selected for this study. All patients had data for both pre-treatment SPECT-CT imaging using  $^{99\text{m}}\text{Tc}$ -MAA as a surrogate of the  $^{90}\text{Y}$ -microspheres treatment and SPECT-CT imaging immediately after the  $^{90}\text{Y}$  activity administration. Pre- and post-treatment doses were computed with TOPAS using the SPECT images to localize the source positions and the CT images to account for tissue inhomogeneities. We compared our results with analytical calculations following the voxel-based MIRD scheme. **Main results.** TOPAS results largely agreed with the MIRD-based calculations in soft tissue regions: the average difference in mean dose to the liver was  $0.14 \text{ Gy GBq}^{-1}$  (2.6%). However, dose distributions in the lung differed considerably: absolute differences in mean doses to the lung ranged from  $1.2$  to  $6.3 \text{ Gy GBq}^{-1}$  and relative differences from 153% to 231%. We also found large differences in the intra-hepatic dose distributions between pre- and post-treatment imaging, but only limited differences in the pulmonary dose. **Significance.** Doses to lung were found to be higher using TOPAS with respect to analytical calculations which may significantly underestimate dose to the lung, suggesting the use of MC methods for  $^{90}\text{Y}$  dosimetry. According to our results, pre-treatment imaging may still be representative of dose to lung in these treatments.

## Introduction

Radioembolization with microspheres containing Yttrium-90 ( $^{90}\text{Y}$ ) is an interventional radiology procedure used to treat both primary and metastatic hepatic malignancies (Kim *et al* 2019). Patients with discrete and identifiable tumors on imaging studies are normally eligible for this treatment (Wehrenberg-Klee *et al* 2019). Typical aims for  $^{90}\text{Y}$  treatment include control of metastatic disease (Gulec *et al* 2007), downstaging of tumor for resection (Lau *et al* 2012), and primary curative treatment (Salem *et al* 2021). To do so,  $^{90}\text{Y}$  microspheres (either glass (Salem *et al* 2004) or resin (Wang *et al* 2017)) with average diameters between 20 and  $60 \mu\text{m}$  are infused into the hepatic arteries so that they circulate across the liver vasculature until they are deposited in end arterioles. The microspheres then emit  $\beta$  particles from  $^{90}\text{Y}$  radioisotope decays, imparting energy to surrounding tissues. These emissions have a continuous energy spectrum, with maximum energy of 2.27 MeV (corresponding to a range of 11 mm in soft tissue) and average energy of 0.937 MeV (corresponding to a range of 2.5 mm in soft tissue); and a half-life of 2.66 d (Gulec *et al* 2006).

As a radiotherapeutical treatment, the absorbed dose in different structures involved should be considered as the main predictor of outcomes for radioembolization by  $^{90}\text{Y}$  (d'Abadie *et al* 2021). However, the process of

radiation dosimetry in these treatments involves several hurdles hampering the determination of dose-response curves (Srinivas *et al* 2014; Chansanti *et al* 2017). First, prior to the administration of the treatment, an angiography of the liver is typically carried out. This allows to map the liver vasculature as well as to check if any aberrant vessels may lead to extrahepatic deposition of activity (van den Hoven *et al* 2014). Angiography is also useful to guide the localization of a catheter for microsphere infusion into the hepatic arteries for treatment. The most basic version of  $^{90}\text{Y}$  dosimetry consists of a rough conversion of infused activity into absorbed dose taking into account the liver or lung mass (Gulec *et al* 2006). Image-based dosimetry allows a more sophisticated and accurate patient-specific dosimetry, either using SPECT or PET imaging to determine activity distributions (O’Doherty 2015). However, image-based dosimetry has its own limitations, as SPECT imaging of  $^{90}\text{Y}$  relies on the bremsstrahlung photons emitted by  $\beta$  particles as they are stopped in tissue. This reduces image resolution due to the lack of clear photopeaks. In addition, other corrections for scattering and attenuation are equally hindered (Kubik *et al* 2021). While PET imaging would overcome many of these challenges, it is not routinely used in clinical practice due to reimbursement challenges.

To overcome these problems, microspheres of macroaggregated albumin (MAA) labeled with  $^{99\text{m}}\text{Tc}$  are first infused as a surrogate for the actual treatment, due to the advantageous properties of  $^{99\text{m}}\text{Tc}$  for SPECT imaging (Campbell *et al* 2009; Kao *et al* 2014). Although these  $^{99\text{m}}\text{Tc}$ -MAA microspheres can vary considerably in size, with diameters of up to  $150\ \mu\text{m}$  (Dezarn *et al* 2011), whereas glass  $^{90}\text{Y}$  microspheres have a diameter of  $15\text{--}35\ \mu\text{m}$  and resin microspheres a diameter between  $20$  and  $60\ \mu\text{m}$ ,  $^{99\text{m}}\text{Tc}$ -MAA microspheres are typically assumed to follow a similar biodistribution (Kennedy *et al* 2007). Despite the difference in size, a correlation between tumor dose using  $^{99\text{m}}\text{Tc}$ -MAA SPECT-based dosimetry and overall survival has been observed (Garin *et al* 2016). Therefore, these pre-treatment studies are used to assess where activity will presumably be deposited and, in particular, whether a significant portion of it goes to the lung, which is a dose limiting organ due to risk of radiation pneumonitis (Wright *et al* 2012). Of note, some studies have shown that  $^{99\text{m}}\text{Tc}$ -MAA intrahepatic distributions can significantly differ from that of  $^{90}\text{Y}$  microspheres, particularly for glass microspheres (Wondergem *et al* 2013).

Assuming that either  $^{90}\text{Y}$ -images are of high enough quality or  $^{99\text{m}}\text{Tc}$ -based pre-treatment images are representative of the actual microsphere distribution, image-based dosimetry can be performed using analytical or Monte Carlo (MC) methods. The analytical method most used in clinical practice is the so-called MIRD formalism or schema which relies on the concept of  $S$ -value, i.e. the absorbed dose in a target per unit activity in a source (Howell 1994). This approach can be, in turn, broken down into different complexity levels. Originally, the MIRD schema considers a compartmental model in which  $S$ -values are defined for organ sources and targets, assuming the activity is uniformly distributed across the organ (Snyder *et al* 1975). For more accuracy, analytical calculations with non-uniform activities can be done by utilizing voxel-wise  $S$ -values (Bolch *et al* 1999), or the dose-point kernel method (Giap *et al* 1995). Nonetheless, these methods do not consider heterogeneities within the patient. By contrast, MC techniques inherently include patient heterogeneities and further improve the accuracy of dose calculations, although at a computational cost. One approach to reduce computation time is to use MC codes, such as MCNPX (Forster and Godfrey 1985) or GATE (Jan *et al* 2004), to obtain radionuclide-specific  $S$ -values or dose-point kernels in soft tissue that can be utilized analytically on a patient-by-patient basis (Villoing *et al* 2017).

Full MC calculations within the patient require the knowledge of the structural components of a patient and their densities. This information can be obtained from CT images, requiring SPECT-CT or PET-CT hybrid imaging to obtain both the source distribution and patient information. Some tools exist that perform full MC calculations for internal dosimetry such as RAYDOSE (Marcatili *et al* 2013), VIDA (Kost *et al* 2015), GAMOS (Amato *et al* 2020; Auditore *et al* 2020) or GATE (Neira *et al* 2020). This work analyzes the dosimetry of 5 patients treated for hepatocellular carcinoma (HCC) with  $^{90}\text{Y}$ -microspheres radioembolization in our institutions, estimating with MC accuracy the dose to the tumors, healthy liver and lung. These patients had pre- and post-treatment SPECT-CT studies allowing us to perform cross comparisons of the estimated dose from the  $^{99\text{m}}\text{Tc}$ -MAA pre-treatment imaging and the actual dose measured with the  $^{90}\text{Y}$  post-treatment imaging. MC calculations are carried out with the TOPAS toolkit (Perl *et al* 2012; Faddegon *et al* 2020), which is a growing framework that wraps up and extends the general purpose code Geant4 (Agostinelli *et al* 2003; Allison *et al* 2006; Allison *et al* 2016), aiming to make MC simulations user-friendly by removing the need for advanced programming skills.

## Methods and materials

### Patient imaging studies

Five patients with HCC treated with  $^{90}\text{Y}$  microspheres between February and July 2021 at the Massachusetts General Hospital were selected for this study. Patients received standard of care pre-treatment SPECT-CT

**Table 1.** Details of pre- and post-treatment imaging and treatment for each patient considered in this study.  $^{90}\text{Y}$  delivery position difference is relative to the  $^{99\text{m}}\text{Tc}$ -MAA catheter position. RHA stands for right hepatic artery; LHA stands for left hepatic artery; CS stands for Couinaud Segment; RAHB stands for right anterior hepatic branch; RPHB stands for right posterior hepatic branch.

	Patient 1	Patient 2	Patient 3	Patient 4	Patient 5
Total $^{90}\text{Y}$ activity (GBq)	1.07	2.69	4.07	3.47	4.48
Type of microsphere	Resin	Resin	Resin	Glass	Glass
$^{99\text{m}}\text{Tc}$ -MAA delivery position	RHA	RHA	RHA	RHA	RHA
$^{90}\text{Y}$ delivery position difference	RHA—18 mm more distal	Split dose: CS VIII and CS VI/VII	Split dose: distal RAHB and RPHB	RHA—15 mm more distal	Split dose: CS VII and CS IV
Days between CT/MR for con- tours & pre-treatment imaging	13 (MR)	21 (CT)	27 (CT)	19 (CT)	18 (CT)
Days between pre- & post- treatment imaging	9	21	8	14	8

imaging, acquired immediately after  $^{99\text{m}}\text{Tc}$ -MAA administration, and post-treatment SPECT-CT imaging acquired immediately after  $^{90}\text{Y}$  microsphere administration. In all cases, angiography was acquired prior to the nuclear medicine study to establish the catheter position for both  $^{99\text{m}}\text{Tc}$ -MAA and  $^{90}\text{Y}$  microsphere infusion. Some differences can be noted among these patients, such as total activity injected, the type of  $^{90}\text{Y}$  microspheres used and the final catheter position for the  $^{90}\text{Y}$  infusion after pre-treatment mapping of liver vasculature and re-adaptation of the plan. Details are specified in table 1.

SPECT images were obtained from 64 planar images with a matrix size of  $256 \times 1024$  pixels and uniformity correction. The voxel size of the 3D reconstructed images was  $5 \text{ mm} \times 5 \text{ mm} \times 5 \text{ mm}$ , the scan length was set to 200 cm and scan speed to  $5 \text{ cm min}^{-1}$ . In all cases, liver and tumors were contoured using the software MiM SurePlan LiverY90 (MiM Software Inc., Cleveland, OH) on the most recent contrast-enhanced cross-sectional imaging of the liver (CT or MR). The type and time between this study and pre-treatment study for each patient are shown in table 1. Deformable image registrations of the liver were performed between the planning image and both pre- and post-treatment SPECT-CT using Plastimatch, a tool for image processing developed at the Massachusetts General Hospital (Sharp *et al* 2010). Due to large differences in patient positioning, a mask with high contrast was added as an additional shell of 5 mm surrounding the liver structures contoured using MiM. This mask was only used for the image registration, not for dose calculations. Deformable image registration was then performed using the B-splines algorithm, optimizing the mean square error as the cost function. This procedure allowed for a direct propagation of the relative position of tumors within the liver from one study to another.

### Dose calculation using voxel-wise S-values (MIRD schema)

Using the intensity (counts) of both pre- and post-treatment SPECT images, we performed analytical calculations using voxel-wise S-values in soft tissue for  $^{90}\text{Y}$ . S-values were taken from the database published by Lanconelli *et al* (2012), corresponding to our voxel size with 5 mm resolution. For this application,  $S(d \leftarrow i)$  is the S-value for a target voxel located a distance  $d$  from a source voxel  $i$ . It specifies the absorbed dose in the target voxel per unit activity in the voxel  $i$ ,  $A_i(t)$ . Therefore, the dose rate at a voxel  $k$  at the time  $t$  is given by

$$\dot{D}_k(t) = \sum_{i=1}^N A_i(t) S(d_k \leftarrow i), \quad (1)$$

where  $N$  represents the total number of voxels and  $j$  represents the distance between the voxel  $k$  and the voxel  $i$ . Under this formalism, S-values are assumed to be constant along time, so that if  $\hat{A} = \int A(t) dt$  is the cumulative activity, the total absorbed dose by the voxel  $k$  is given by

$$D_k = \int_{t_0}^{\infty} \dot{D}_k(t) dt = \sum_{i=1}^N \int_{t_0}^{\infty} A_i(t) dt S(d_k \leftarrow i). \quad (2)$$

As the  $^{90}\text{Y}$  microspheres are used to embolize vessels, it is assumed here that all the activity is delivered locally, i.e. there is neither biological washout nor activity redistribution after imaging. In that case, equation (2) can be rewritten as

$$D_k = \sum_{i=1}^N \frac{A_{0,i}}{\lambda} S(d \leftarrow i) \quad (3)$$

where  $A_{0,i}$  is the initial activity at the voxel  $i$  and  $\lambda = 0.258 \text{ d}^{-1}$  is the decay constant for  $^{90}\text{Y}$  emissions. A normalization condition is introduced as  $A_0 = \sum_i A_{0,i}$ , where  $A_0$  is the total activity infused, assuming all the activity administered is contained within the SPECT image. In this work we used this condition to report total

absorbed dose per unit activity administered,  $D/A_0$ . Once dose was calculated using the SPECT image, a 3D interpolation process was performed to obtain doses in CT-based matrixes. The interpolation method used the inverse of the distance between each node in the CT matrix and the 8 closest nodes in the SPECT matrix to weight the contribution from each SPECT matrix node. This application has also been developed for this study and it is publicly available at <https://github.com/mghro/MIRDCalculation>. Doses were scaled to consider only the activity within the patient, using the threshold  $HU > -900$  in the CT studies to determine voxels belonging to the patient anatomy. This threshold was determined after visual inspection to make sure air outside the patient was not included but lungs were.

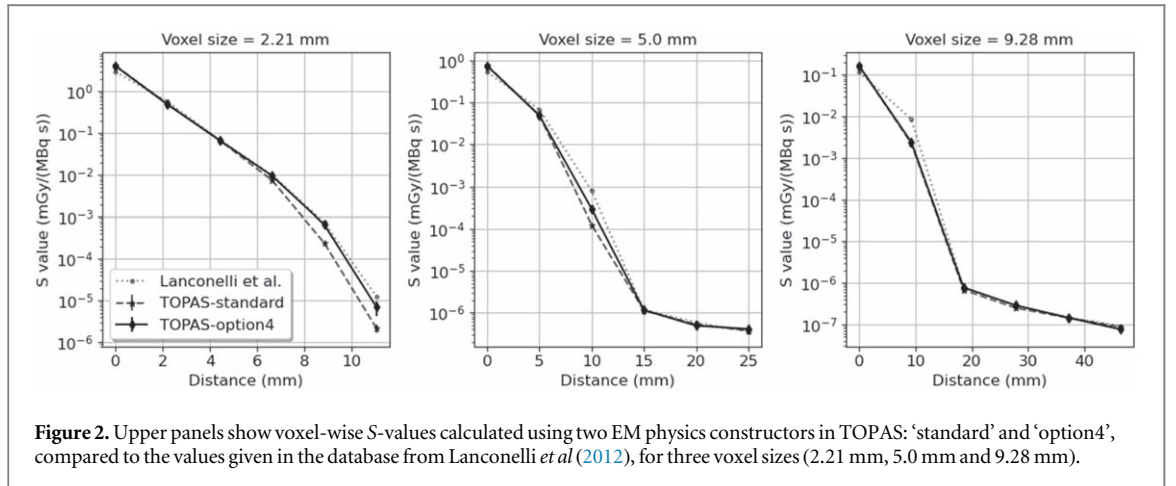
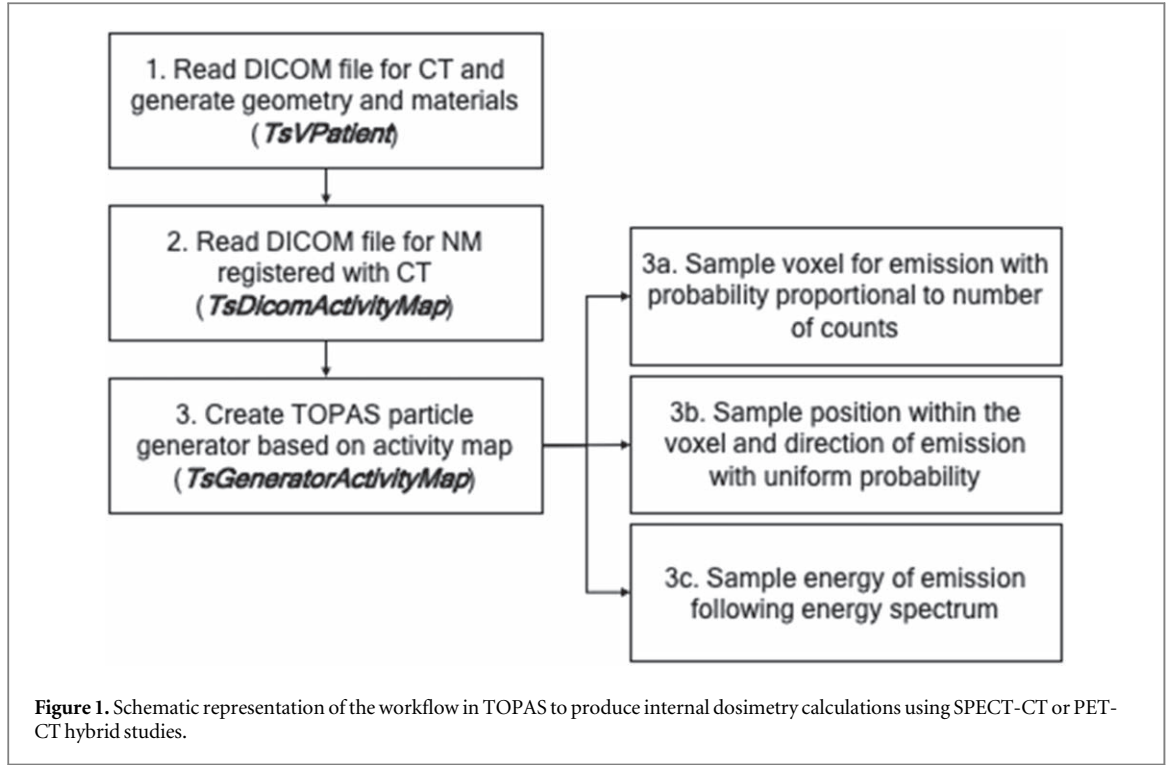
### Dose calculation using TOPAS

TOPAS (Perl *et al* 2012; Faddegon *et al* 2020) is a wrapped and extended version of the Geant4 (Agostinelli *et al* 2003; Allison *et al* 2006; Allison *et al* 2016) Monte Carlo toolkit specifically focused on medical physics. While TOPAS makes use of the broadly validated physics models and the architecture of Geant4, multiple tools have been developed by the TOPAS community aiming at simplifying MC simulations for medical physicists and radiation oncologists without expertise on coding. TOPAS uses *geometry components* to specify shapes and materials, *particle sources and generators* to initiate radiation, *modular physics lists* to specify what physics interactions and cross sections are considered and *scorers* to tally and measure quantities of interest. A user can create a simulation in TOPAS with a simple text file following a syntax based on parameters. For instance, some ready-to-use tools are geometrical shapes and complex nested structures, scoring of radiotherapy relevant quantities, and time features, i.e. the ability of handling motions of all components of the simulation. TOPAS interprets DICOM files, such as CT scans, as well as contours or dose distributions stored as DICOM-RT standard. A DICOM-based CT scan is generated as a geometry component in TOPAS, following a voxelized geometry with twofold purpose: assigning a given material to each voxel and serving as the reference to score absorbed dose. For the former, TOPAS uses the method proposed by Schneider *et al* (2000) and the correction proposed by Paganetti *et al* (2008) to associate Hounsfield Units and material composition, employing 25 different tissue-based materials and densities.

We developed two new classes in TOPAS (v3.7) to read nuclear medicine DICOM files, such as SPECT or PET images. The first one is a geometry component, *TsDicomActivityMap*, which serves to position the SPECT image, i.e. activity map, relative to the patient geometrical object, created from the CT images. Positions for voxels with counts higher than a given threshold in the nuclear medicine image (0 for this work) are then recorded. The second one is a particle source and generator, *TsGeneratorActivityMap*, which generates the particles emitted by radionuclides. To simulate one history, first a voxel from *TsDicomActivityMap* is selected with a probability proportional to its number of counts. Then, the position of the emission is uniformly sampled within the voxel, and a direction is isotropically sampled. Finally, a given emission is selected for the considered radionuclide, i.e. particle and energy of emission. For  $^{90}\text{Y}$ , only electrons are considered following the emission spectrum taken from the RADAR database (Stabin and Da Luz 2002). Figure 1 shows a diagram of the process followed in TOPAS for the implementation of internal dosimetry calculations. A simulation is then run in TOPAS by using a simple parameter text file, for which the user only has to specify the radionuclide employed, the path of the CT and NM DICOM files, the number of decays to be simulated and the physics lists to be employed. The internal dosimetry feature will be publicly available for the TOPAS community in future releases of the code.

TOPAS can employ any of the reference physics lists already contained in the Geant4 toolkit. Users can specify what models are used to represent different physical processes as a trade-off between accuracy and speed depending on the application. The default electromagnetic (EM) physics constructor of Geant4 uses the Coulomb model for single scattering and the Urban model for multiple scattering of electrons with kinetic energy up to 100 MeV (Ivanchenko *et al* 2011). However, option 4 of the EM physics constructor of Geant4 offers the highest accuracy for electron tracking, using the Goudsmit-Saunderson model for multiple scattering for up to 100 MeV electrons and more detailed models for ionization and bremsstrahlung for low-energy electrons (Allison *et al* 2016). In order to test the validity of the default EM physics constructor for our application, we calculated the  $S$  values for  $^{90}\text{Y}$  emissions in soft tissue, as defined by the ICRU Report 44 (White *et al* 1989), using TOPAS with both default and ‘option 4’ EM physics constructors. Our results were compared to those obtained by Lanconelli *et al* (2012).

Using the default EM physics constructor, we simulated  $10^7$  histories for each patient, which represents a total initial activity of  $A_0 = 10$  MBq. Results provided by TOPAS simulations in this context represent the dose rate per 10 MBq of activity at the time of imaging,  $\dot{D}_0/10$  MBq. In order to calculate the total absorbed dose at  $t \rightarrow \infty$ , a similar operation as done in equations (2)–(3) is performed as:

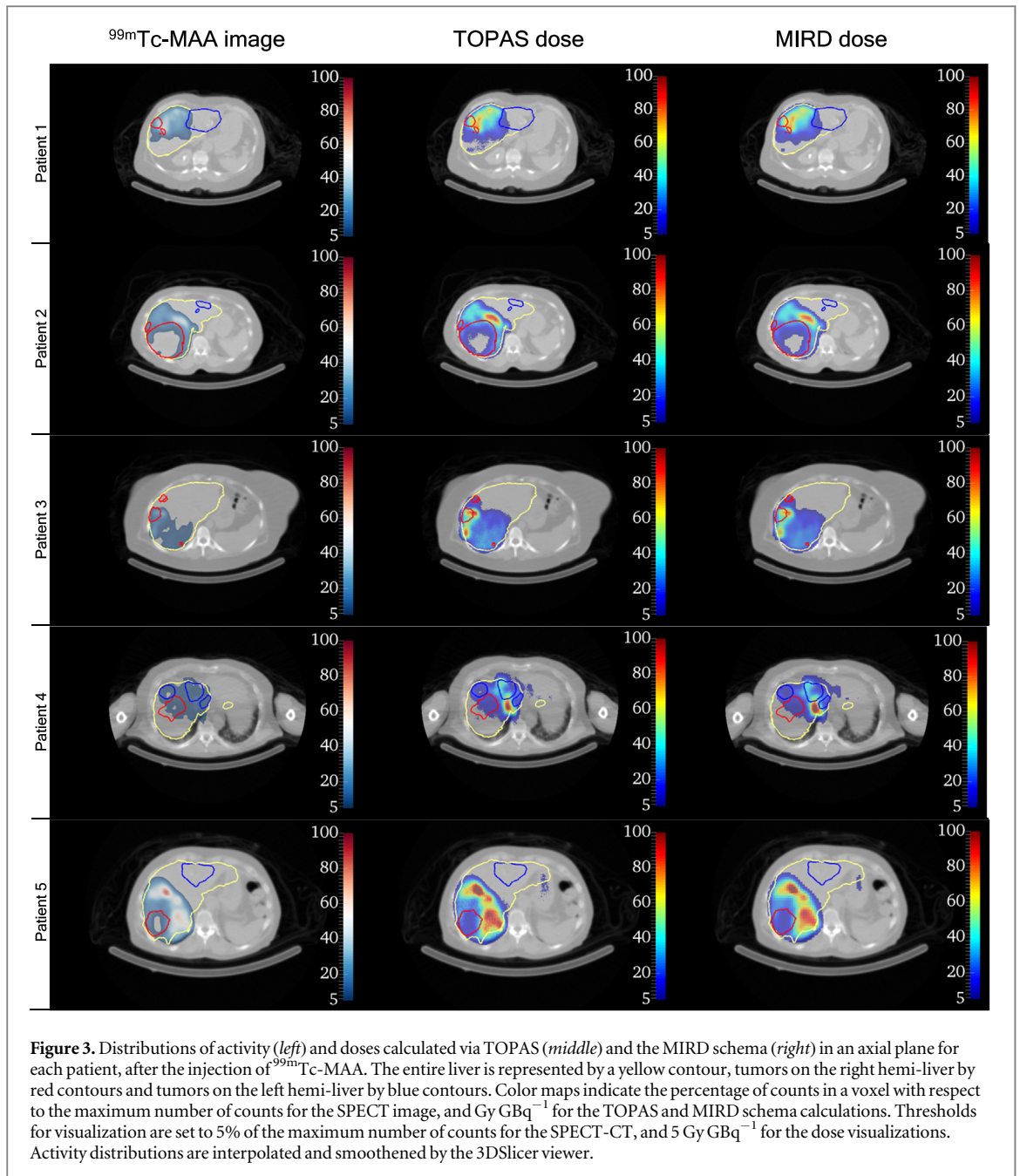


$$\frac{D}{A_0} = \frac{1}{A_0} \int_{t_0}^{\infty} \dot{D}(t) dt = \frac{\dot{D}_0/10 \text{ MBq}}{\lambda} \quad (4)$$

## Results

S values for  $^{90}\text{Y}$  were calculated using TOPAS with both the standard and 'option 4' EM physics constructors for three voxel sizes, 2.21, 5 and 9.28 mm, so that they can be compared to three of the datasets from Lanconelli *et al* (2012). Figure 2 shows the comparison between these values.

Differences between default and 'option4' physics in TOPAS were within 1.5% for the self-irradiated voxel (i.e. distance = 0) in all cases, for all voxel sizes. Maximum differences for the smallest voxel size scaled up to -65% around 10 mm, which represents the maximum range for the electrons emitted under the continuous slow-down approximation. Relative differences at about this distance increased with larger voxels, although the absolute S values also decreased for larger voxels. Of note, while the simulation of  $10^7$  emissions took 30 min on average for the default EM physics constructor using a single iMac (3.5 GHz processor, 32 GB memory), this time went up to 42 h for the 'option 4' EM physics constructor, i.e. about 85 times longer. Database values from



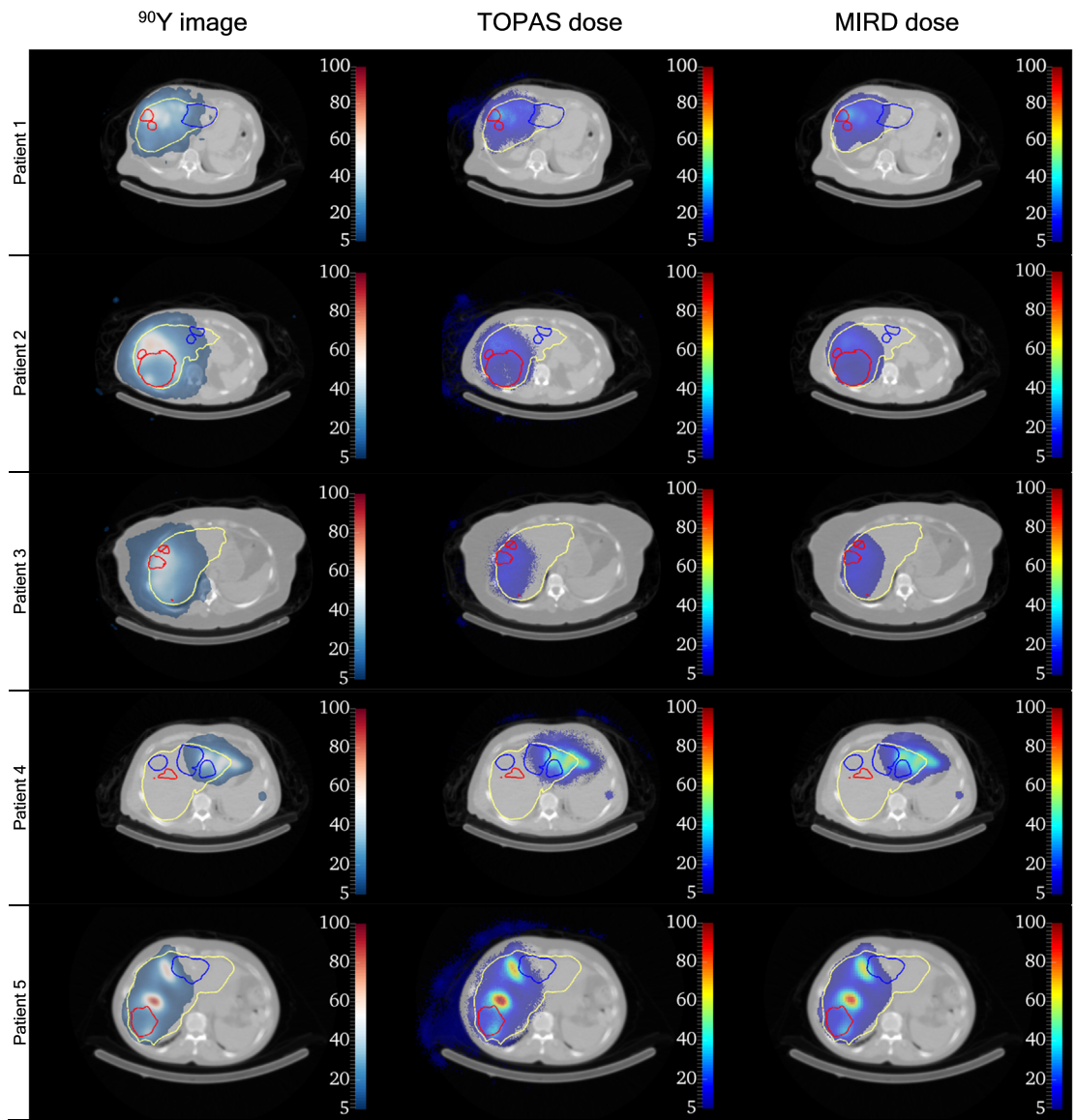
Lanconelli *et al* (2012) showed an approximate 30% decreased dose to the self-irradiated voxel, which seemed to be compensated by increased doses in immediately surrounding voxels. These differences may be due to discrepancies in both the physics models, the definition of soft tissue employed or geometrical specifications. Statistical uncertainties in the doses for the 5 mm voxel size ranged from 0.006% for the self-irradiated voxel to 7% at 5 voxels distance (i.e. 25 mm). Using 10 MBq, for patient calculations in high-dose regions, where voxels emit between 0.001% and 0.01% of the total activity, uncertainty to the self-absorbed dose was estimated at around 0.9%. Uncertainties at low-dose regions are greater.

Figure 3 shows the SPECT-CT images for pre-treatment studies for each patient, as well as MIRD schema and TOPAS calculations of absorbed dose per unit activity administered.

By contrast, figure 4 shows SPECT-CT images and dose calculations according to both methods for the post-treatment studies in approximately the same axial planes.

Differences in lung doses using TOPAS and MIRD are illustrated on figure 5, which shows an axial slice of the pre-treatment CT study for patient 1. Similar results are observed for the other patients as well as in post-treatment studies.

Figure 6 shows a comparison of the cumulative dose-volume histograms (DVHs) (per unit activity) obtained in tumors in both hemi-livers (left tumors and right tumors), right lung and the entire liver when using TOPAS



**Figure 4.** Distributions of activity (*left*) and doses calculated via TOPAS (*middle*) and the MIRD schema (*right*) in an axial plane for each patient, after SPECT imaging of the  $^{90}\text{Y}$  microspheres used as treatment. The entire liver is represented by a yellow contour, tumors on the right hemi-liver by red contours and tumors on the left hemi-liver by blue contours. Color maps indicate the percentage of counts in a voxel with respect to the maximum number of counts for the SPECT image, and  $\text{Gy GBq}^{-1}$  for the TOPAS and MIRD schema calculations. Thresholds for visualization are set to 5% of the maximum number of counts for the SPECT-CT, and  $5 \text{ Gy GBq}^{-1}$  for the dose visualizations. Activity distributions are interpolated and smoothed by the 3DSlicer visualizer.

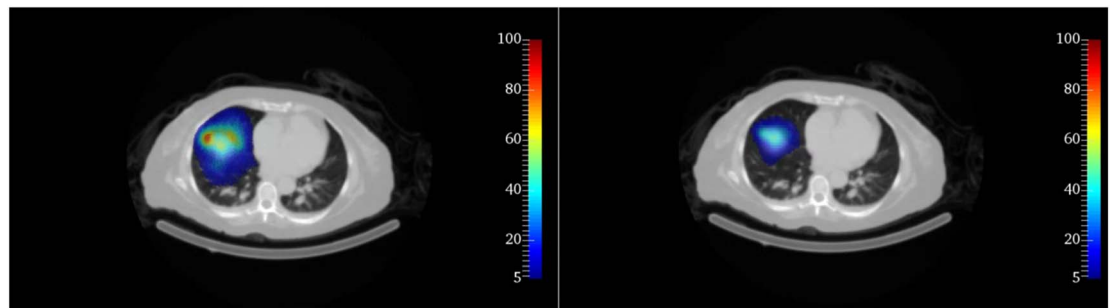


**Figure 5.** Example of the differences for the calculated dose to lung using TOPAS (*left*) and MIRD scheme (*right*) for the pre-treatment imaging-based dosimetry of Patient 1. Color maps indicate  $\text{Gy GBq}^{-1}$  for the TOPAS and MIRD schema calculations.

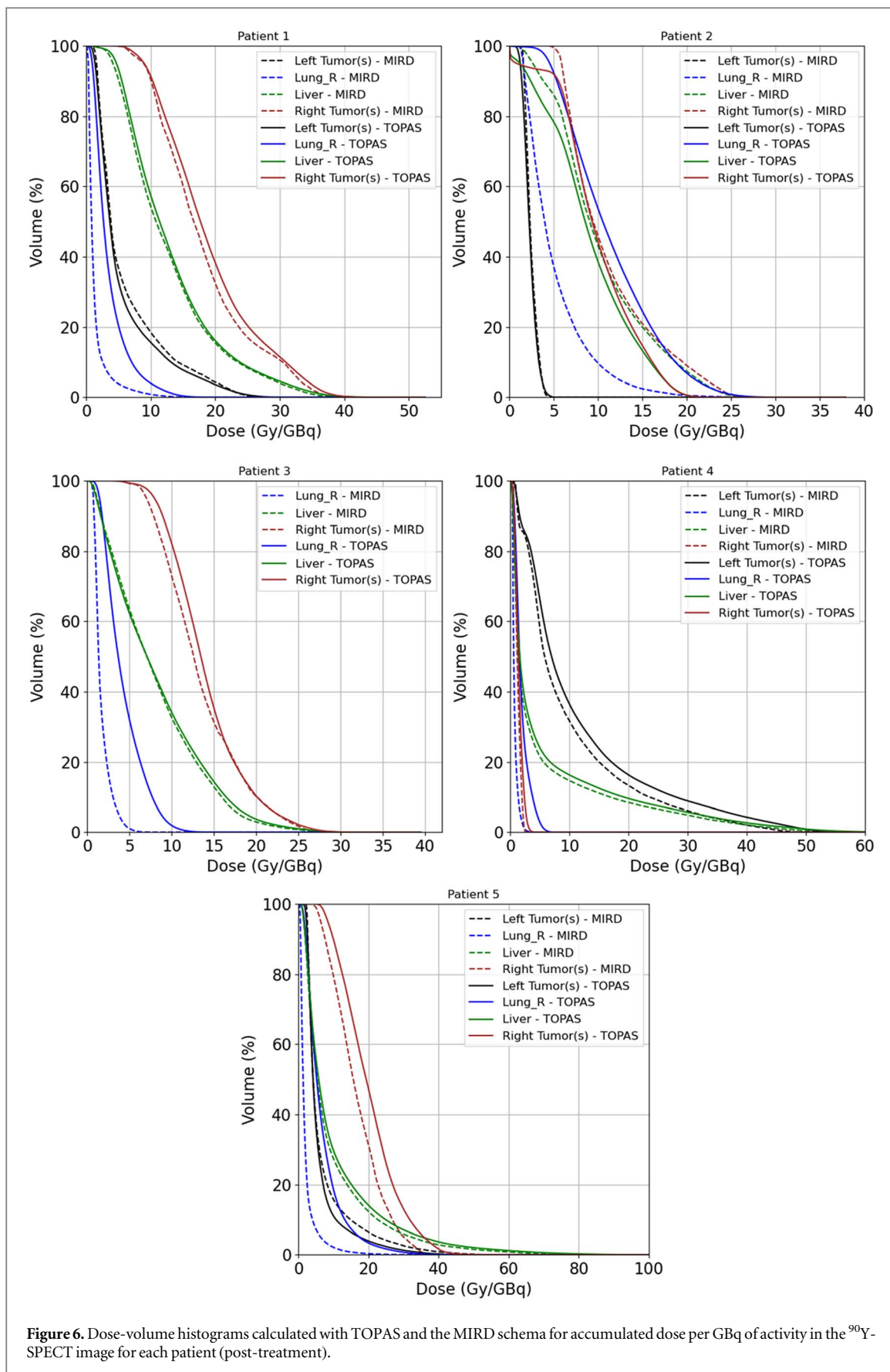


**Figure 6.** Dose-volume histograms calculated with TOPAS and the MIRD schema for accumulated dose per GBq of activity in the  $^{90}\text{Y}$ -SPECT image for each patient (post-treatment).

and MIRD dosimetric methods. The actual  $^{90}\text{Y}$  SPECT-CT studies were used for this comparison. As expected, dose to lung was underestimated using analytical methods due to the lack of consideration of tissue heterogeneities. For the rest of structures considered, no clear trend in differences between MC and MIRD schema was observed.

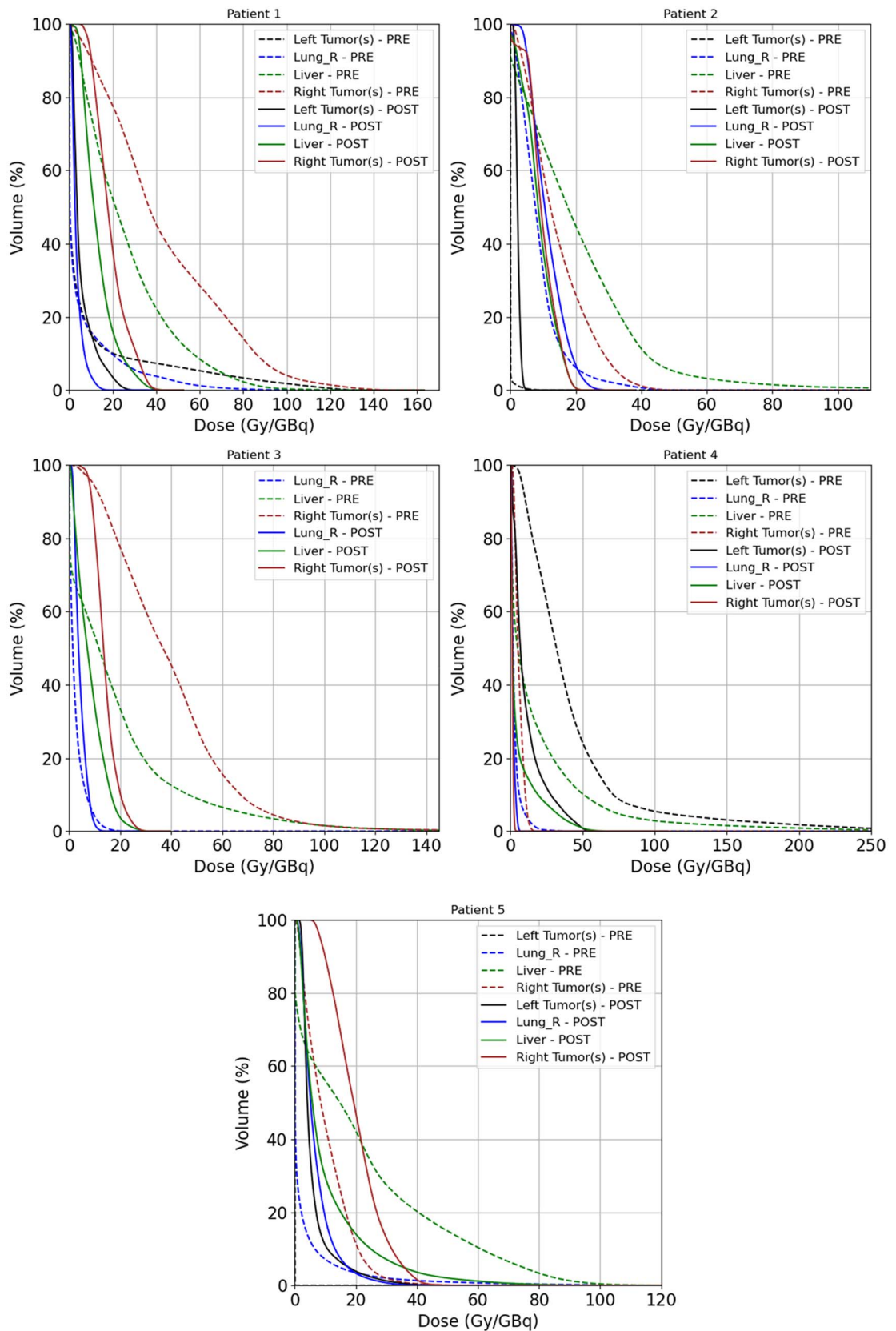


**Figure 7.** Dose-volume histograms calculated with for accumulated dose per GBq of activity in both the  $^{99m}\text{Tc}$ -MAA-SPECT and  $^{90}\text{Y}$ -SPECT images for each patient (pre versus post-treatment).

Additionally, figure 7 shows the DVHs calculated with MC techniques (TOPAS) for pre- and post-treatment images to illustrate the possibility of using pre-treatment imaging to assess the actual dose distributions with  $^{90}\text{Y}$  microspheres.

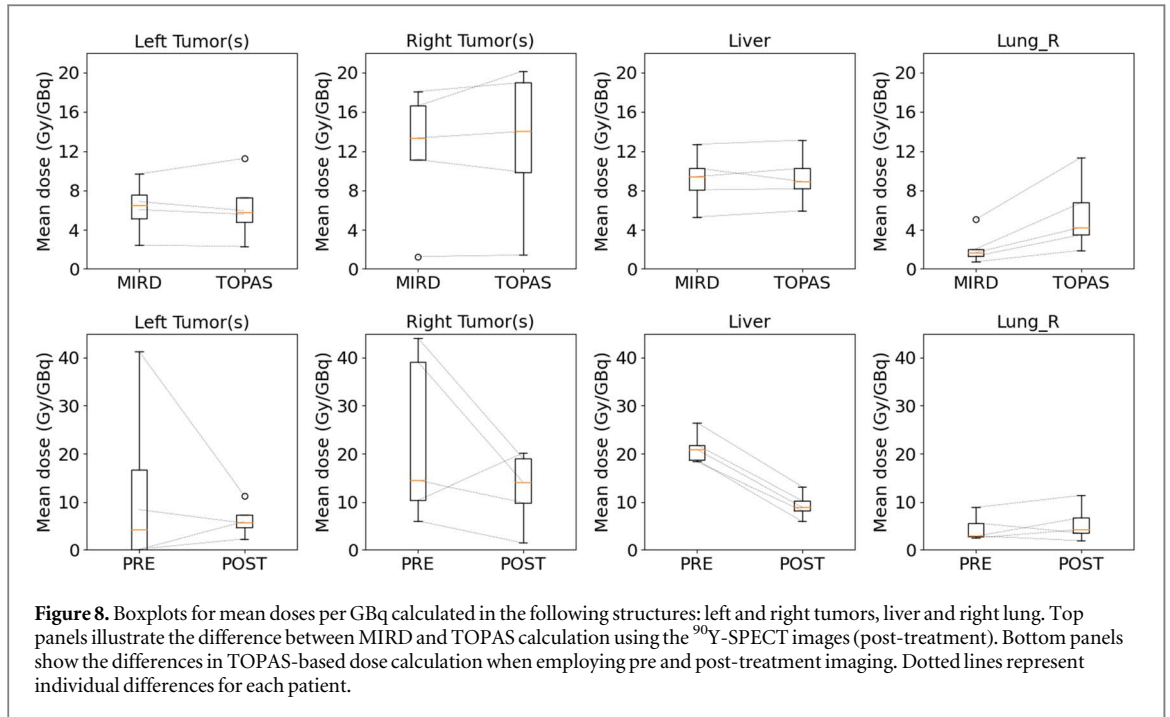


Figure 8 summarizes results for all patients in terms of mean dose to the considered structures, i.e. the whole liver, right and left tumors and right lung. Differences between analytical and Monte Carlo calculations are stressed in the top panels, where a significant difference is shown for lung, but good agreement is found for liver and tumors. The bottom panels illustrate the discrepancies between pre- and post-treatment imaging-based dosimetry.

## Discussion

Two main points have been addressed in this work: (a) what are the differences between MC and analytical methods to calculate dosimetry for  $^{90}\text{Y}$ -based radioembolization -particularly for lung-; and (b) how do pre- and post-treatment image-based dosimetry differ. Both have been previously studied: for example, Auditore *et al* (2020) evaluated the differences between GAMOS and a convolution kernel method, although not for lung shunt. Allred *et al* (2018) evaluated differences between pre- and post-treatment SPECT-CT images using a phantom instead of patient data. This work combines all these elements: we provide MC-accurate quantitative data for tumor, healthy tissue and lung dosimetry comparing pre- and post-treatment SPECT-CT. TOPAS has been used for the MC calculations with the standard EM physics constructor of Geant4 rather than the more accurate ‘option4’, provided that differences in calculation times were up to two orders of magnitude higher and dose differences were small for the major portion of the absorbed dose (concentrated on the self-irradiated and adjacent voxels). As a toolkit with multiple useful developments for medical physics, TOPAS incorporates a method to classify HU from a CT study into 25 different tissue-like materials following the approach by Schneider *et al* (2000), in contrast with other MC implementations in which only 4–5 materials are used (Mikell *et al* 2015; Auditore *et al* 2020). Differences in mass densities and materials have been recently shown to be important for lung dose (Kim *et al* 2021).

Differences for (a) can be seen in the dose distribution overlaid on the CT images in figures 3–5 and in terms of accumulated dose per unit activity in figure 6. As analytical methods typically do not consider differences in tissue composition, they were expected to underestimate dose to lung due to its low density. Our results confirm this premise, showing a significant increase in doses to lung for all patients when MC calculations are used. In particular, differences of mean calculated dose to the lung differed between methods from 1.2 to 6.3 Gy GBq<sup>-1</sup> (or 153% to 231% in relative values), with an average difference of 3.4 Gy GBq<sup>-1</sup> (or 168% in relative values). This result is in line with previous studies comparing soft tissue kernels without correcting by density with calculations using the MC.DOSXYZnrc code (Mikell *et al* 2015). In fact, this may carry clinical consequences, as one of the main limiting factors for  $^{90}\text{Y}$  treatment eligibility is the lung shunt fraction (LSF), i.e. the fraction of activity deposited within the lungs. LSF is typically evaluated directly on SPECT imaging or using analytical methods to compute dose. Dose calculation guidelines limit the dose received after a single  $^{90}\text{Y}$  treatment to 30 Gy, and the cumulative total dose to 50 Gy. Our results show that the actual LSF may be underestimated if MC

techniques are not used. This finding suggests that the recommended pulmonary dose threshold may be more commonly exceeded than realized. Consequently, since the reported side effects with the currently employed calculation scheme are not exceeding expectation, the actual tolerable LSF limits may be higher for  $^{90}\text{Y}$  treatments than the limit used in current clinical practice. However, due to respiratory motion and the long time required for SPECT acquisitions, the actual biodistribution of activity in lungs is likely blurred or averaged along the patient motion, so that the voxel-based calculations might be affected. This effect can be particularly important near the lung-liver interface in the instance that high activity is concentrated over that area of the liver. These factors complicate lung dosimetry and as recently acknowledged by the European Association of Nuclear Medicine (EANM) Dosimetry Committee, determining limits for lung dose remain a completely open problem (Chiesa *et al* 2021).

Additionally, Patient 5 showed significant differences in doses to the tumors in the right side of the liver, up to 21% higher when using MC calculations. As shown in figure 4, uptake of patient 5 showed a pronounced peak in a small region near the right tumors on the right (inferior) part of the liver. Such a pattern, together with the uncertainties due to the interpolation of the dose grid, might introduce partial volume effects when using analytical methods using voxel-wise  $S$ -values, which can result in an underestimation of the dose in the contiguous voxels as shown in patient 5. However, as shown in figure 2,  $S$ -values from the Lanconelli *et al* (2012) database underestimate the dose to the source voxel with respect to TOPAS, which also contributes to enhanced differences when activity peaks in single voxels. In situations with activity uptake distributed over larger regions, TOPAS and MIRD schema-based calculations were within comparable accuracy, as partial volume effects are not observed and differences in the self-irradiated voxels between TOPAS and Lanconelli *et al* (2012) are compensated by the contributions to the dose from activity in the surrounding voxels. For instance, mean doses to the liver did not exceed  $1.4 \text{ Gy GBq}^{-1}$  (or 13% in relative values) for any patient, with an average difference of  $0.14 \text{ Gy GBq}^{-1}$  (or 2.6% in relative values) between MC and MIRD-schema calculations.

As for point (b) pre- and post-treatment image-based dosimetry, significant differences were observed between the dose distribution predicted by the pre-treatment images and the actual dose distribution calculated upon  $^{90}\text{Y}$  images, as illustrated in the bottom panels of figure 8. For example, the D50 in the target was up to a factor 4 (for patient 4) higher when using pre-treatment images. This is likely due to the change of the catheter position after assessing pre-treatment images (see table 1), which significantly changes the pathways of the infused activity through the vasculature. In this specific instance, a left-sided tumor included in the  $^{99\text{m}}\text{Tc}$ -MAA injection was not treated with  $^{90}\text{Y}$  during this session. Overall, these results also demonstrate the necessity of using voxel-based dosimetry instead of compartmental models for  $^{90}\text{Y}$ -microsphere radioembolization as distributions of activity are far from being uniform in liver sub-regions (Hashikin *et al* 2017).

Other factors also contribute to this disparity:  $^{99\text{m}}\text{Tc}$ -MAA microspheres are inherently different from  $^{90}\text{Y}$  microspheres. This may result in the two microsphere types being preferentially deposited in different vessels (Van De Wiele *et al* 2012). Note that differences in doses to tumors are notable for all patients, as shown in figure 7, as differences in biodistributions of activity from pre- to post-treatment images are mainly due to changes on the catheter position within the liver. However, doses to the lung evaluated in pre- and post-treatment images showed a good agreement, as observed in the phantom study by Allred *et al* (2018). In fact, as shown in figure 8, using analytical methods instead of MC techniques produced greater discrepancies than using pre-treatment dosimetry in the estimation of the dose to the lung. This seems to support the use of pre-treatment imaging to estimate LSF as extrahepatic shunts are probably not as affected as intrahepatic biodistribution by changes in delivery positions within the liver.

In addition to studying dosimetry for  $^{90}\text{Y}$  microsphere treatments, this work also presents TOPAS as a powerful MC tool to perform internal dosimetry for radiopharmaceutical treatments. Besides providing access to complex MC calculations to nuclear medicine and medical physics users without expertise in programming, a growing body of extensions of TOPAS are being developed in potentially relevant fields for internal dosimetry. Examples of these are the microdosimetry extension (Zhu *et al* 2019), the brachytherapy toolkit (Berumen *et al* 2021) or the nano-scale radiobiological project TOPAS-nBio (Schuemann *et al* 2019). Our implementation of a SPECT-based source in TOPAS assumes a uniform activity within a given voxel but the electron tracks are still simulated at a smaller scale, sampled by default randomly within the voxel, which can be seen by the granularity of the dose distributions with TOPAS in figures 3 and 4. Note that any other assumption or model of intra-voxel activity is also implementable using TOPAS. Interestingly, the versatility of the TOPAS architecture allows for non-uniform activity distributions, as well as potential breakdowns of a voxel (macroscopic scale) into smaller structures like those developed in the TOPAS-nBio project. Although in this work we have employed  $^{90}\text{Y}$  microspheres which are assumed to remain immobile, internal dosimetry for other radiopharmaceutical treatments involves the time evolution of the activity administered. Time features are already integrated in TOPAS, which can be of great help in these situations. The current version presented in this work is, however, limited to dose calculation from a static SPECT

image. The development of more flexible internal dosimetry tools is a potential future workline for the TOPAS team.

## Conclusions

TOPAS results showed comparable doses to the entire liver and tumors, but a significantly greater dose to lungs than predicted by the voxel-level MIRD. This suggests the importance of using MC techniques to assess lung shunt fraction in radiopharmaceutical treatments. Dosimetry predicted by pre-treatment imaging was compared to that from post-treatment imaging, showing significant intrahepatic differences due to changes in the delivery position within the liver. However, dose to lung due to lung shunt fraction was comparable for pre- and post-treatment imaging. Therefore, pre-treatment images were found to be potentially useful for estimating dose limits for organs at risk (e.g. lung).

## Funding

This work was in part supported by the National Institutes of Health/National Cancer Institute (NIH/NCI grant no. U24 CA 215123: ‘The TOPAS Tool for Particle Simulation, a Monte Carlo Simulation Tool for Physics, Biology and Clinical Research’). Alejandro Bertolet is supported by the NIH/NCI grant no. K99 CA267560. Eric Wehrenberg-Klee is supported by the NIH/NCI grant K08 CA 245257.

## Conflicts of interest

Eric Wehrenberg-Klee receives preclinical research funding, clinical research funding, and consulting fees from Boston Scientific, and consulting fees and honoraria from Sirtex. The other authors have no conflict of interests to declare.

## Ethics approval

Formal consent was not required for this study.

## ORCID iDs

Alejandro Bertolet  <https://orcid.org/0000-0002-9890-693X>  
Eric Wehrenberg-Klee  <https://orcid.org/0000-0002-4712-3986>  
Mislav Bobić  <https://orcid.org/0000-0002-9409-8680>  
Clemens Grassberger  <https://orcid.org/0000-0002-4425-4489>  
Joseph Perl  <https://orcid.org/0000-0002-9446-3131>  
Harald Paganetti  <https://orcid.org/0000-0002-6257-2413>  
Jan Schuemann  <https://orcid.org/0000-0002-7554-8818>

## References

- Agostinelli S *et al* 2003 Geant4—a simulation toolkit *Nucl. Instrum. Methods Phys. Res. A* **506** 250–303
- Allison J *et al* 2006 Geant4 developments and applications *IEEE Trans. Nucl. Sci.* **53** 270–8
- Allison J *et al* 2016 Recent developments in Geant4 *Nucl. Instrum. Methods Phys. Res. A* **835** 186–225
- Allred J D, Niedbala J, Mikell J K, Owen D, Frey K A and Dewaraja Y K 2018 The value of 99mTc-MAA SPECT/CT for lung shunt estimation in 90Y radioembolization: a phantom and patient study *EJNMMI Res.* **8** 50
- Amato E *et al* 2020 Full Monte Carlo internal dosimetry in nuclear medicine by means of GAMOS *J. Phys.: Conf. Ser.* **1561** 012002
- Auditore L *et al* 2020 Monte Carlo 90Y PET/CT dosimetry of unexpected focal radiation-induced lung damage after hepatic radioembolisation *Phys. Med. Biol.* **65**
- Berumen F, Ma Y, Ramos-Méndez J, Perl J and Beaulieu L 2021 Validation of the TOPAS Monte Carlo toolkit for HDR brachytherapy simulations *Brachytherapy.* **20** 911–21
- Bolch W E *et al* 1999 MIRD pamphlet no. 17: the dosimetry of nonuniform activity distributions - Radionuclide S values at the voxel level *J. Nucl. Med.* **40** 11S–36S
- Campbell J M, Wong C O, Muzik O, Marples B, Joiner M and Burmeister J 2009 Early dose response to yttrium-90 microsphere treatment of metastatic liver cancer by a patient-specific method using single photon emission computed tomography and positron emission tomography *Int. J. Radiat. Oncol. Biol. Phys.* **74** 313–20
- Chansanti O *et al* 2017 Tumor dose response in yttrium-90 resin microsphere embolization for neuroendocrine liver metastases: a tumor-specific analysis with dose estimation using SPECT-CT *J. Vascular Intervent. Radiol. SIR* **28** 1528–35

- Chiesa C *et al* 2021 EANM dosimetry committee series on standard operational procedures: a unified methodology for <sup>99m</sup>Tc-maa pre- and <sup>90</sup>Y peri-therapy dosimetry in liver radioembolization with <sup>90</sup>Y microspheres *EJNMMI Phys.* **8** 77
- d'Abadie P *et al* 2021 Prediction of tumor response and patient outcome after radioembolization of hepatocellular carcinoma using <sup>90</sup>Y-PET-computed tomography dosimetry *Nucl. Med Commun.* **42** 747–54
- Dezarn W A *et al* 2011 Recommendations of the American association of physicists in medicine on dosimetry, imaging, and quality assurance procedures for <sup>90</sup>Y microsphere brachytherapy in the treatment of hepatic malignancies *Med. Phys.* **38** 4824–45
- Faddegon B *et al* 2020 The TOPAS tool for particle simulation, a Monte Carlo simulation tool for physics, biology and clinical research *Phys Medica.* **72** 114–21
- Forster R A and Godfrey T N K 1985 MCNP - A General Monte Carlo code for neutron and photon transport *Monte-Carlo Methods and Applications in Neutronics, Photonics and Statistical Physics* (Berlin : Springer ) pp 33–55
- Garin E, Rolland Y, Laffont S and Edeline J 2016 Clinical impact of <sup>99m</sup>Tc-MAA SPECT/CT-based dosimetry in the radioembolization of liver malignancies with <sup>90</sup>Y-loaded microspheres *Eur. J. Nucl. Med. Mol. Imaging* **43** 559–75
- Giap H B, Macey D J, Bayouth J E and Boyer A L 1995 Validation of a dose-point kernel convolution technique for internal dosimetry *Phys. Med. Biol.* **40** 365–81
- Gulec S A, Mesoloras G, Dezarn W A, McNeillie P and Kennedy A S 2007 Safety and efficacy of Y-90 microsphere treatment in patients with primary and metastatic liver cancer: the tumor selectivity of the treatment as a function of tumor to liver flow ratio *J. Transl. Med.* **5** 1–9
- Gulec S A, Mesoloras G and Stabin M 2006 Dosimetric techniques in <sup>90</sup>Y-microsphere therapy of liver cancer: the MIRD equations for dose calculations *J. Nucl. Med.* **47** 1209–11
- Hashikin N A A *et al* 2017 Systematic investigation on the validity of partition model dosimetry for <sup>90</sup>Y radioembolization using monte carlo simulation *Phys. Med. Biol.* **62** 7342–56
- van den Hoven A F, Smits M L J, de Keizer B, van Leeuwen M S, van den Bosch MAAJ and Lam MGEH 2014 Identifying aberrant hepatic arteries prior to intra-arterial radioembolization *Cardiovascular Interventional Radiol.* **37** 1482–93
- Howell R W 1994 The MIRD schema: from organ to cellular dimensions *J. Nucl. Med.* **35** 531–3
- Ivanchenko V *et al* 2011 Recent improvements in Geant4 electromagnetic physics models and interfaces *Prog Nucl. Sci. Technol.* **2** 898–903
- Jan S *et al* 2004 GATE : a simulation toolkit for PET and SPECT *Phys. Med. Biol.* **49** 4543–61
- Kao Y H *et al* 2014 Personalized predictive lung dosimetry by technetium-<sup>99m</sup> macroaggregated albumin SPECT/CT for yttrium-90 radioembolization *EJNMMI Res.* **4** 1–12
- Kennedy A *et al* 2007 Recommendations for radioembolization of hepatic malignancies using yttrium-90 microsphere brachytherapy: a consensus panel report from the radioembolization brachytherapy oncology consortium *Int. J. Radiat. Oncol. Biol. Phys.* **68** 13–23
- Kim S P, Cohalan C, Kopeck N and Enger S A 2019 A guide to <sup>90</sup>Y radioembolization and its dosimetry *Phys. Med.* **68** 132–45
- Kim S P, Juneau D, Cohalan C and Enger S A 2021 Standardizing SPECT/CT dosimetry following radioembolization with yttrium-90 microspheres *EJNMMI Phys.* **8** 71
- Kost S D, Dewaraja Y K, Abramson R G and Stabin M G 2015 VIDA: A voxel-based dosimetry method for targeted radionuclide therapy using Geant4 *Cancer Biotherapy Radiopharm.* **30** 16–26
- Kubik A *et al* 2021 Evaluation of qualitative and quantitative data of Y-90 imaging in SPECT/CT and PET/CT phantom studies *PLoS One* **16** 1–16
- Lanconelli N *et al* 2012 A free database of radionuclide voxel S values for the dosimetry of nonuniform activity distributions *Phys. Med. Biol.* **57** 517–33
- Lau W Y *et al* 2012 Patient selection and activity planning guide for selective internal radiotherapy with yttrium-90 resin microspheres *Int. J. Radiat. Oncol. Biol. Phys.* **82** 401–7
- Marcatili S *et al* 2013 Development and validation of RAYDOSE: A Geant4-based application for molecular radiotherapy *Phys. Med. Biol.* **58** 2491–508
- Mikell J K, Mahvash A, Siman W, Mourtada F and Kappadath S C 2015 Comparing voxel-based absorbed dosimetry methods in tumors, liver, lung, and at the liver-lung interface for <sup>90</sup>Y microsphere selective internal radiation therapy *EJNMMI Phys.* **2** 1–14
- Neira S *et al* 2020 Quantification of internal dosimetry in PET patients: individualized monte carlo versus generic phantom-based calculations *Med. Phys.* **47** 4574–88
- O' Doherty J 2015 A review of 3D image-based dosimetry, technical considerations and emerging perspectives in <sup>90</sup>Y microsphere therapy *J. Diagn. Imaging Ther.* **2** 1–34
- Paganetti H, Jiang H, Parodi K, Slopesma R and Engelsman M 2008 Clinical implementation of full Monte Carlo dose calculation in proton beam therapy *Phys. Med. Biol.* **53** 4825–53
- Perl J, Shin J, Schumann J, Faddegon B and Paganetti H 2012 TOPAS: An innovative proton monte carlo platform for research *Med. Phys.* **39** 6818–37
- Salem R *et al* 2004 Use of Yttrium-90 glass microspheres (therasphere) for the treatment of unresectable hepatocellular carcinoma in patients with portal vein thrombosis *J. Vascular Intervent. Radiol.* **15** 335–45
- Salem R *et al* 2021 Yttrium-90 radioembolization for the treatment of solitary, unresectable HCC: the legacy study *Hepatology.* **0** 1–11
- Schneider W, Bortfeld T and Schlegel W 2000 Correlation between CT numbers and tissue parameters needed for monte carlo simulations of clinical dose distributions *Phys. Med. Biol.* **45** 459–78
- Schuemann J *et al* 2019 TOPAS-nBio: an extension to the TOPAS simulation toolkit for cellular and sub-cellular radiobiology *Radiat. Res.* **191** 125–38
- Sharp G *et al* 2010 Plastimatch: an open source software suite for radiotherapy image processing *Proc XVI<sup>th</sup> Int Conf use Comput Radiother*
- Snyder W S, Ford M R, Warner G G and Watson S B 1975 *MIRD Pamphlet No. 11: Absorbed Dose Per Unit Cumulate Activity for Selected Radionuclides and Organs* (New York, NY: Society of Nuclear Medicine)
- Srinivas S M *et al* 2014 Determination of radiation absorbed dose to primary liver tumors and normal liver tissue using post radioembolization <sup>90</sup>Y PET *Front Oncol.* **4** 1–12
- Stabin M G and Da Luz L C Q P 2002 Decay data for internal and external dose assessment *Health Phys.* **83** 471–5
- Villoing D, Marcatili S, Garcia M P and Bardies M 2017 Internal dosimetry with the monte carlo code gate: validation using the ICRP/ICRU female reference computational model *Phys. Med. Biol.* **62** 1885–904
- Wang E A, Stein J P, Bellavia R J and Broadwell S 2017 Treatment options for unresectable HCC with a focus on SIRT with Yttrium-90 resin microspheres *Int. J. Clin. Pract.* **71** 1–15
- Wehrenberg-Klee E, Gandhi R T and Ganguli S 2019 Patient selection and clinical outcomes of Y90 in hepatocellular carcinoma *Tech. Vascular Intervent. Radiol.* **22**, 70–3

- White D R, Booz J, Griffith R V, Spokas J J and Wilson I J 1989 ICRU Report 44, tissue substitutes in radiation dosimetry and measurements *J. Int. Commun. Radiat Units Meas.* **23** 1–189
- Van De Wiele C *et al* 2012 SIRT of liver metastases: physiological and pathophysiological considerations *Eur. J. Nucl. Med. Mol. Imaging* **39** 1646–55
- Wongergem M *et al* 2013 <sup>99m</sup>Tc-macroaggregated albumin poorly predicts the intrahepatic distribution of <sup>90</sup>Y resin microspheres in hepatic radioembolization *J. Nucl. Med.* **54** 1294–301
- Wright C L *et al* 2012 Radiation pneumonitis following yttrium-90 radioembolization: case report and literature review *J. Vascular Intervent. Radiol.* **23** 669–74
- Zhu H *et al* 2019 The microdosimetric extension in TOPAS: development and comparison with published data *Phys. Med. Biol.* **64** 0–15